Electrode-Dependent Spin and Thermoelectric Transport in M@C_{80} (M = Fe, Co, Ni) Molecular Junctions

Alaa A. Al-Jobory[1], Sameer Nawaf[1*], Anhar A. Ouda[1], Ali Ismael[2]

[1] *Department of Physics, College of Science, University of Anbar, Ramadi, Iraq.*

[2] *Department of Physics, Lancaster University, Lancaster LA1 4YB, UK.*

Corresponding author: Email: Sameer@uoanbar.edu.iq

Abstract:

The ability to engineer molecular junctions with tunable spin and thermoelectric properties is central to the development of high-performance nanoscale devices. In this work, we investigate endohedral fullerenes M@C80 (M = Fe, Co, Ni) contacted by gold and graphene electrodes using density functional theory combined with the non-equilibrium Green's function formalism. Encapsulation of transition-metal atoms inside the C_{80} cage induces pronounced charge transfer, orbital hybridization, and spin splitting, leading to strongly modulated and energy-selective transmission spectra. The Au–Fe@C_{80}–Au junction exhibits the highest spin polarization and near-unity transmission at the Fermi level, making it particularly suitable for spintronic applications. In contrast, the Gr–Co@C_{80}–Gr junction displays an exceptionally large thermoelectric response. The thermoelectric figure of merit is reaching ZT >1000 which originates from sharp, asymmetric transmission resonances near the Fermi energy and enhanced $\pi - \pi$ coupling with graphene. These values represent upper theoretical limits within a coherent electronic transport regime and do not imply a violation of thermodynamic constraints, as the thermoelectric efficiency remains bounded by the Carnot limit. The Ni@C_{80} junction shows broader transmission features, which are favorable for energy-selective transport. A comparative analysis of electrode materials reveals that gold provides stronger and more stable molecule–electrode coupling with higher electrical conductance, whereas graphene enables superior energy filtering and an enhanced Seebeck response.

Keywords: *Endohedral fullerenes; Molecular junctions; Charge transfer; Nanostructured thermoelectric; Spin-dependent transport*

1. Introduction

Fullerenes are among the most attractive nanomaterials in recent decades due to their unique hollow sphere-shaped structure composed of carbon atoms linked by lines of π bonds, making them chemically stable and electronically distinct[1]. Examples of these molecules are C_{60}, C_{70}, C_{80}, and so on. C_{60} and C_{80} have quite different structures and characteristics among of the most recognized carbon fullerenes. C_{80} is notable by its larger size and capacity to hold atoms or ions while C_{60} is known for its high stability and perfect geometric symmetry[2]. Also, HOMO-LUMO gap of C_{80} is smaller than the gap of C_{60} which increases its chemical activity and qualifies it for heat transport applications[3]. C_{80} is more frequently utilized in energy and advanced nanomaterials although C_{60} is frequently used in electronics, solar cells, and antioxidants[4]. Moreover, C_{60} is easy to study due to its structural stability. However, C_{80} offers more application flexibility due to its structural versatility.

Endohedral fullerenes are one or more atoms of a specific element are enclosed in a carbon cage to produce new properties not present in the pure fullerenes[5]. In this case, one or more atoms of a specific element are trapped inside fullerenes without broking the carbon's cage bonds. The formula $M@C_x$ is frequently used to refer to endohedral fullerenes where M is the confined atom or ion and C_x is the carbon cage of x carbon atoms. Usually, transition metals and rare earth elements are among the most regularly utilized atoms in endohedral fullerenes.

Charges within the molecule are reorganized as a result of the interaction between the inserted atom and the carbon cage, which frequently involves a charge transfer from the atom to the cage or vice versa [6,7]. This process gives the endohedral molecules unique properties not found in the pure fullerenes. A specific type of these molecules is $M@C_{80}$ where M stands for one of the transition metals, such as nickel (Ni), cobalt (Co), or iron (Fe). These three elements were chosen since they have unfilled d-levels, and they are all part of the same period (period 4) of the periodic table. The unfilled d-levels give them unique magnetic properties and capacity to interact with electrons. The electron configuration of Iron, Cobalt, and Nickel atoms are $4s^2\ 3d^6$, $4s^23d^7$, and $4s^23d^8$ respectively. Because of its well-known strong ferromagnetic characteristics, Iron is perfect for researching how the magnetic moment inside the carbon cage affects electron transitions[8–10]. Cobalt is famous by its relative stability in nanostructures and its capacity to adjust electron energy levels near the Fermi level [11]. Nickel effectively enhances thermal transport efficiency because of its relatively balanced electronic interactions, despite having a comparatively lower magnetic moment[12].

Doping these metals into the C_{80} cage causes notable changes in the electronic configuration and magnetic spin states, making them an interesting area in molecular device's applications. Many studies have shown that the attendance of transition metals within fullerenes leading to the appearance of new thermoelectric and magnetic properties. *Oda et al.* investigated the thermoelectric properties of $M@C_{60}$ where M = Co, Ni[13]. The study showed that doping C_{60} with transition metals (Co and Ni) increased the Seebeck (S) and thermal efficiency. *S. Sarfaraz et al.* studied the electronic properties of ($M@C_{60}$) (M = Sc, Ti, V, Cr, Mn, Fe, Co, Ni, Cu & Zn) for strong hydrogen evolution reaction[14]. The results of the study showed that doping with a transition metal significantly changes the electronic properties of ($M@C_{60}$) complexes. *Serkan Caliskan* used first principles calculations to examine spin and electronic properties of $X@C_{70}$ (X = N, B) based molecular devices[15]. The study showed that $X@C_{70}$ molecules cause spin-asymmetry and Au-N@C_{70}-Au device displays a nearly linear I-V curve, suggesting a metallic behavior. *Tianwei He et al.* utilized DFT to expect endohedral $M@C_{60}$ (M = Li, Na, K, Rb, Cs, Ca, Sc, Ti, V, Cr, Mn, Fe, Co, Ni, Cu, Sr, Y, Zr, Nb and Ag) fullerenes as capable high performance hydrogen evolution reaction[16]. The study showed that the charge transfer from metal atom to C_{60} improved the charge distribution of the C_{60} cage which enhances the adsorption of H-atom. *S. Tawfik et al.* used first principles calculations to examine the adsorption of many gases on ($M@C_{60}$, M = Ca, Na and Sr)[17]. The results showed that the I-V characteristics of Au-Na@C_{60}-Au and Au-Ca@C_{60}-Au structures leads to significant change in conductivity.

Experimental evidence for endohedral metallofullerenes has been demonstrated by X-ray diffraction confirming the metal atom inside the fullerene cage[18]. Moreover, functionalized C_{60} derivatives with encapsulated metals have been structurally characterized, providing further experimental support for metal-encaged fullerenes[19]. Although molecular transport studies have explored C_{60} and its derivatives, the spin and thermoelectric transport literature for molecular junctions of $M@C_{80}$ is surprisingly scarce. For $M@C_{80}$, there are but a few reports, such as those on $Sc_3N@C_{80}$ electrodes connected to gold, that have explored control of thermopower via molecular orientation or pressure and have observed bi-thermoelectric behavior due to narrow resonances near the Fermi level. However, systematic studies correlating spin-

polarized transport and thermoelectric efficiency parameters are largely uncharted. It is largely because of the experimental difficulties in preparing stable $M@C_{80}$ junctions and computational difficulties in calculating coupled spin and heat transport via first-principles methods.

Using a quantum computational methodology such as density functional theory (DFT) and non-equilibrium Green's Function (NEGF), the system's electronic, magnetic, and thermoelectric behavior would be calculated and compared under different conditions. This study shows how these three elements affect the electronic, magnetic, and thermoelectric properties of the molecule when connected to metallic electrodes such as gold (Au) or semi-metallic electrodes such as graphene (Gr). Graphene is famous by its high flexibility and quick electron mobility while gold is well-known for its superior conductive qualities and chemical stability[20].

The aim of selecting the electrode type is to compare the system's performance with varying electronic conductivity and electronic structure. The interaction between the molecule and the electrode involve charge transfer, electronic interference, and even the impact of the doped metal on the magnetic moment. Analyzing the molecule's effectiveness in converting thermal energy into an electric current are further objectives of the study. This makes it possible to use these systems in applications such as thermoelectric generators or Nano coolers.

Theoretical Part:

Density Functional Theory (DFT) combined with Non-equilibrium Green's Function (NEGF) method used to determine the electronic, magnetic, and thermoelectric characteristics of the molecules under investigation. The electron exchanges in the system were described by the PBE (Perdew–Burke–Ernzerhof) function, which is a subset of the GGA (Generalized Gradient Approximation) function[21,22]. The total energy and molecular geometry optimization were performed using the SIESTA program[23]. The optimized geometry of the endohedral C_{80} cage was found by applying different atomic configurations to determine the lowest energy structure. In each case, the molecule relaxed until the overall force across each atom was less than 0.04 V/Ang. The plane wave basis cutoff energy is fixed at approximately 200 Ry for lattice and structural relaxation.

The Gollum program was used to analyze the transport details of the molecule when connected to metallic (gold) or two-dimensional (graphene) electrodes[24]. The systems that have been represented are nearly one-dimensional. The metalloid-endohedral C_{80} fullerene is placed between two semi-infinite electrodes (gold or graphene) as shown in Figure 1. Electron transport is evaluated along the device's longitudinal axis (z-direction), which comprises both the electrodes and the molecule. The graphene sheet's armchair orientation determines the direction of electron transport in graphene electrode-based systems. In the present calculations, electron–phonon interactions are not explicitly included. The transport is therefore treated within the coherent elastic regime, which is a widely adopted approximation for molecular junctions under low-bias and near-equilibrium conditions. While vibrational effects may introduce quantitative corrections at higher bias or temperature, they are not expected to qualitatively change the main transport trends discussed here. A fully inelastic treatment including electron–phonon coupling is left for future work.

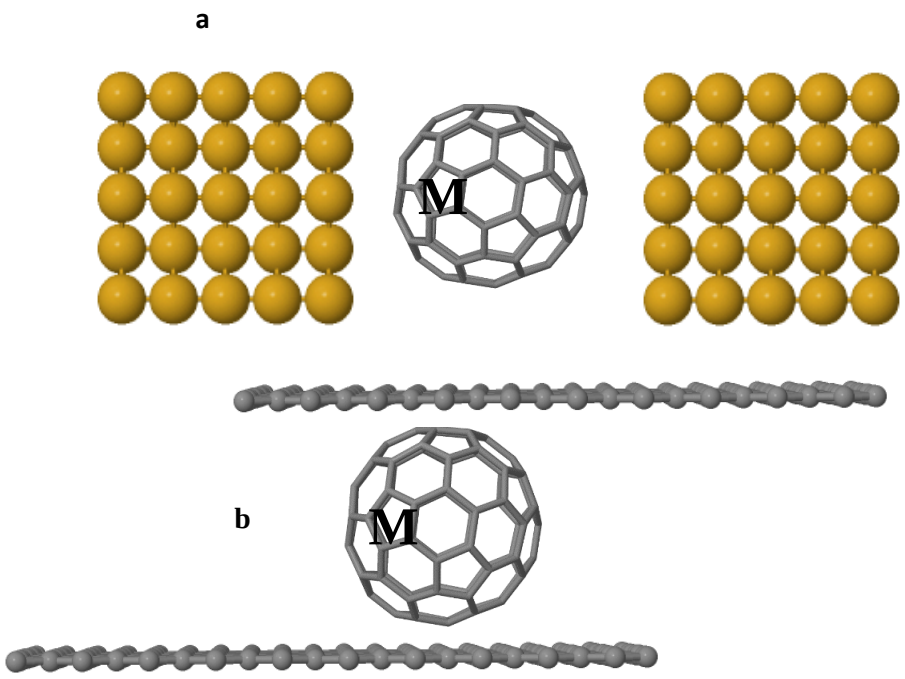

Figure 1: (a) The structure of M@C_{80} connecting the gold electrode, (b) the structure of M@C_{80} connecting the Gr electrode

The transmission coefficient T(E) offers information about the possibility of electron transmission across the M@C_{80} junction, demonstrating quantum transport behavior and energy-dependent conduction channels[25]. The electrical conductance G is computed using the Landauer formula[26]:

$$G = G_o \int_{-\infty}^{\infty} T(E)\left(-\frac{\partial f}{\partial E}\right) dE \qquad (1)$$

Where $G_o = \frac{2e^2}{h}$ refers to the quantum conductance, and $\left(-\frac{\partial f}{\partial E}\right)$ represents Fermi-Dirac distribution derivative.

The Seebeck coefficient S is specified by the equation:

$$\mathrm{S(E)} = -\frac{1}{\mathrm{eT}}\frac{\mathrm{L_1}}{\mathrm{L_o}} \qquad (2)$$

Where

$$L_i = \int_{-\infty}^{\infty} dEp(E)(E - E_F)^i \qquad (3)$$

The integral is obtained L_0, L_1, L_2 at $i = 0,1,2$, respectively.

The thermoelectric figure of merit ZT is given by the equation.

$$ZT = \frac{GS^2}{\kappa}T \qquad (4)$$

The thermal conductance κ_e is calculated by the equation[3]:

$$\kappa_e = \frac{2}{h} \int_{-\infty}^{\infty} (E - E_f)^2 T(E) \left(-\frac{\partial f}{\partial E}\right) dE \quad (5)$$

2. Results and Discussion

The degree of electron coupling and localization within the system can be seen through Electron Localization Function (ELF) analysis. ELF is essential for identifying magnetic interactions brought on by the encapsulated transition metals[27]. The density of states close to the Fermi level is simultaneously determined by the charge distribution, which shows how electrons are moved from the metal atom to the fullerene cage or vice versa[28]. In order to design M@C_{80} based nanostructures with improved magnetic functionality and optimized thermoelectric behavior, it is possible to use the microscopic understanding of how encapsulated atoms control electronic structure that is provided by ELF and charge distribution calculations.

The charge density contour maps for (a) pure C_{80}, (b) Fe@C_{80}, (c) Co@C_{80}, and (d) Ni@C_{80} are shown in Figure 2(a-d). A delocalized π-electron system of fullerenes is presented by the symmetrical distribution of charge density around the carbon as shown in (Fig. 2a). Even electronic surroundings are indicated by the contour lines surrounding each carbon atom that are uniformly spaced. There is a noticeable change in charge density with Fe doping (Fig. 2b), particularly in the area surrounding the encapsulated Fe atom. The contours are denser around the Fe site, representing a localized electron density concentration and strong Fe hybridization with the surrounding carbon atoms. Although the charge density is still concentrated near the Co atom in the case of Co@C_{80} (Fig. 2c), there appears to be less interaction because the perturbation is smaller than in the case of Fe@C_{80}.

Ni@C_{80} system (Fig. 2d) displays a smoother contour curve and a more diffused density surrounding the Ni atom in different behavior of Fe and Co. This tendency may indicate a decrease in charge transfer or orbital overlapping from Fe to Ni. The difference in electronegativities and electronic structures of the metal atoms causes the differences in electron localizations[29]. These charge distribution differences are anticipated to influence electronic and magnetic properties of the systems, such as their nanoelectronics or thermoelectric device performance. Additionally, the electron localization near the central dopant can be traced back to the extent of donation or back-donation between the C_{80} cage and the dopant. The redistribution and accumulation of charges can also be responsible for the reactivity and stability of such endohedral fullerenes.

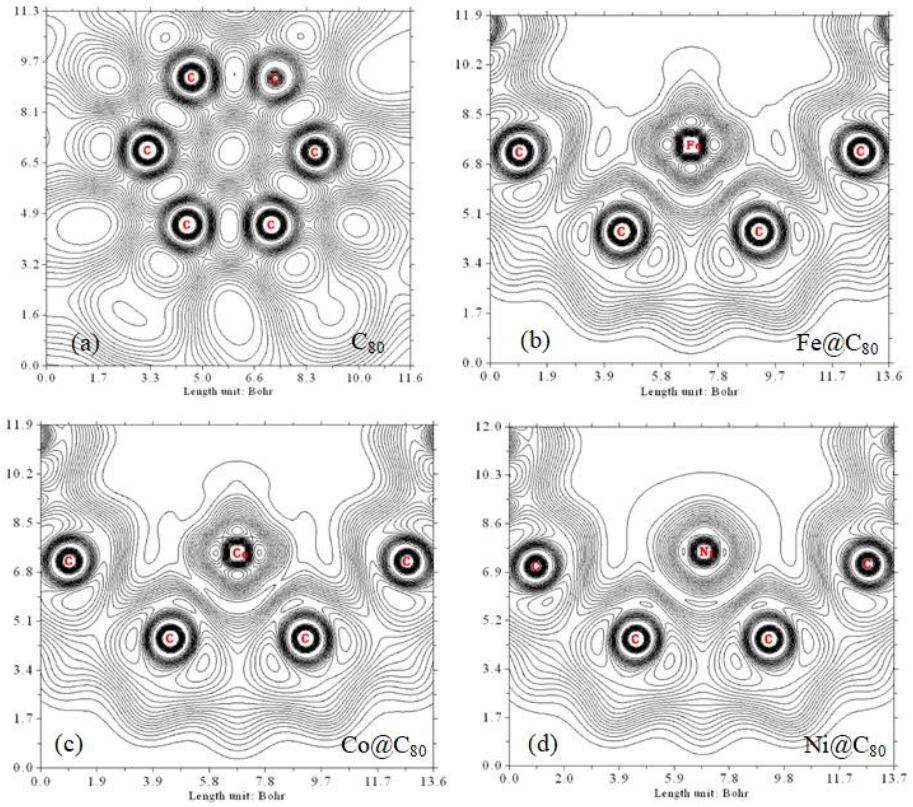

Figure 2(a-d): The charge density contour plots for (a) pristine C_{80}, (b) $Fe@C_{80}$, (c) $Co@C_{80}$, and (d) $Ni@C_{80}$.

Figure 3(a-d) illustrates the Electron Localization Function (ELF) plots of (a) pristine C_{80}, (b) $Fe@C_{80}$, (c) $Co@C_{80}$, and (d) $Ni@C_{80}$. In (Fig. 3a), pristine C_{80} contains high ELF values (red regions) in the vicinity of carbon atoms, which shows a high degree of electron localization due to the covalent C–C bonding network. ELF's symmetrical and uniform distribution in C_{80} suggests homogeneous bonding and electronic delocalization on the cage surface[30]. Upon encapsulation of Fe (Fig.3b), a strong distortion of ELF, especially around the metal atom, is observed, where the electron localization is decreased (blue-green regions), representing charge delocalization and close metal–cage interaction Fe d-orbitals hybridizing with the cage π-system is suggested by ELF damping around Fe. A balance between covalent interaction and electron delocalization is shown in the case of $Co@C_{80}$ (Fig. 3c). The ELF surrounding the Co atom is more localized with moderate localization. This could indicate a partial charge transfer from Co to the cage and a comparatively stable electronic configuration. The ELF plot indicates even less interaction with the cage for $Ni@C_{80}$ where localization around the Ni atom is decreased as shown in (Fig. 3d). The ELF variations for Fe, Co, and Ni originated from the difference of their electron configurations and bonding nature. These variations in the electron localization also show different magnetic and catalytic activities for each doped system. The ELF reduction from Fe to Ni shows the weakening of metal–cage electronic coupling, which may affect their relative stability and reactivity. The 3D surface also shows the depth and distribution of ELF maxima, corroborating localized electron clouds in the neighborhood of C atoms of the undoped system and their redistribution in doped derivatives. The more distorted ELF surfaces of the doped systems also indicate the perturbation introduced by the encapsulated atoms. The charge density distribution and the electron localization function plots were evaluated using Multiwfn program[31,32].

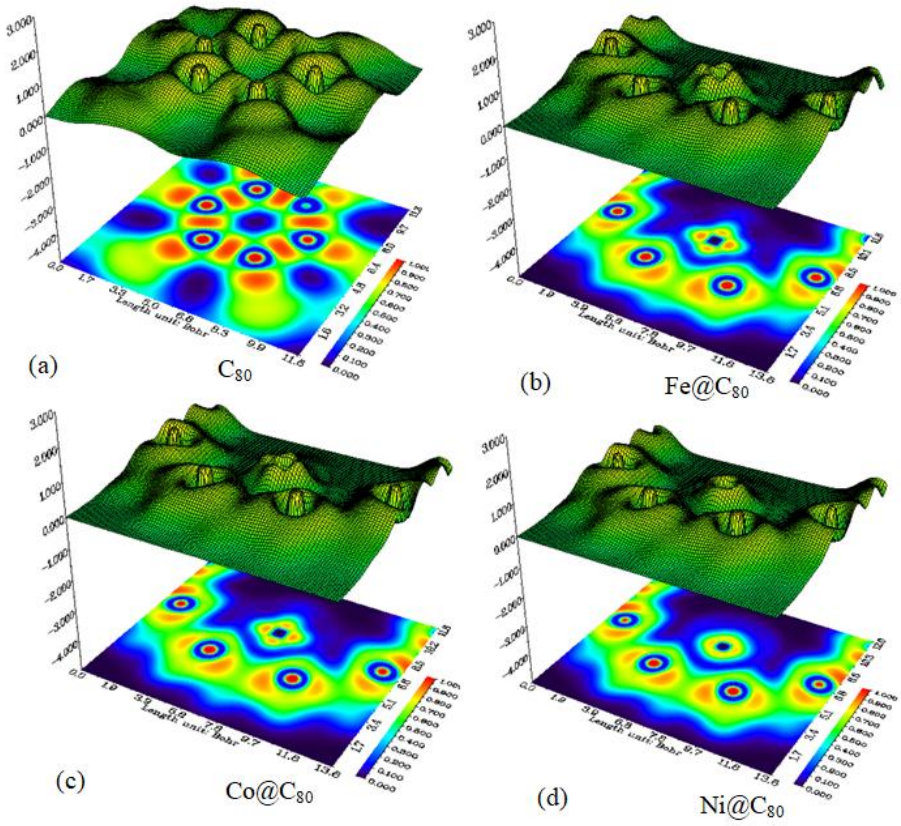

Figure 3(a-d): The Electron Localization Function (ELF) plots for (a) pristine C_{80}, (b) $Fe@C_{80}$, (c) $Co@C_{80}$, and (d) $Ni@C_{80}$

Figure 4(a,b) illustrates the transmission coefficient T(E) for $M@C_{80}$ (M = Fe, Co, Ni) between gold electrodes and graphene electrodes. The sharp transmission dips observed near the Fermi level are characteristic signatures of destructive quantum interference arising from phase cancellation between multiple molecular orbitals participating in coherent transport[33]. In gold electrodes (Fig. 4a), for all doped systems ($Fe@C_{80}$, $Co@C_{80}$, and $Ni@C_{80}$), the transmission is significantly greater than that of pristine C_{80}. $Fe@C_{80}$ has intense and sharp peaks near the Fermi level (0-0.5 eV) referring to a high hybridization between gold states and Fe-based molecular orbitals. $Co@C_{80}$ shows a less sharp profile with moderate peaks at 0.2 eV, indicating good but weak coupling. $Ni@C_{80}$, though with less acute characteristics near the Fermi level, has wider and higher transmission at high energies (1.3–1.8 eV), which would be suitable for high-energy carrier conduction. Such behavior shows that gold electrodes are well coupled with $M@C_{80}$ systems, leading to effective charge transmission.

In comparison, graphene electrodes (Figure 4b) yield smaller magnitudes of transmission throughout the energy range, via smaller π–π or orbital overlap with the fullerene cage[34]. $Fe@C_{80}$ leads the doped systems once more, with a peak transmission in the 0.2–0.7 eV range, but much smaller than the gold case. $Co@C_{80}$ possesses a flat and damped profile, indicating minimal interaction with graphene. Unexpectedly, $Ni@C_{80}$ shows a steep step-like increase at near 1 eV, possibly resonant alignment with the graphene Dirac point, but otherwise low transmission. In this work, E_F^{DFT} denotes the Fermi energy obtained self-consistently from the DFT calculations and represents the chemical potential separating occupied and unoccupied Kohn–Sham states at zero temperature. For pristine, charge-neutral graphene, E_F^{DFT} coincides with the Dirac point. However, in realistic systems, including functionalized graphene, reduced graphene

oxide, or graphene interacting with adsorbates, defects, or electrodes, charge redistribution can occur, leading to a shift of the Fermi level away from the Dirac point[35]. In the present system, such interactions modify the electronic structure, and therefore E_F^{DFT} should not be generally interpreted as the Dirac point. Instead, it serves as the appropriate reference energy for analyzing the electronic structure and transport properties of the full system. These results imply that while doping benefits performance for both sorts of electrodes, the size and shape of T(E) are considerably related to contact type. Gold electrodes, in general, produce superior orbital coupling and transport characteristics over graphene electrodes for all three dopants. Of all the doped systems, Fe@C_{80} transmits the nearest Fermi level and therefore is the optimal choice, particularly when in conjunction with gold electrodes for electronic or thermoelectric applications.

In both cases, the transmission coefficient T(E) drops abruptly in the energy range 0.4–1.6 eV, marking the transport gap equal to the molecular HOMO-LUMO gap. In the gold electrode system (a), pristine C_{80} displays a relatively wide gap with low transmission at the Fermi level, indicating semiconducting behavior. The transport gap is reduced when transition metals (Fe, Co, and Ni) are added. Ni@C_{80} shows the largest reduction, indicating increased hybridization and metallic-like conductivity. In particular, Fe@C_{80} displays enhanced transmission at energies above the Fermi level with LUMO-dominated conduction, whereas that of Co@C_{80} is roughly symmetric around the gap center with a contribution from both HOMO and LUMO states being equal. T(E) drops below 10^{-6} in the graphene electrode system, representing larger transport barriers especially for Fe@C_{80} and Ni@C_{80}. The LUMO levels are slightly higher energies than the gold electrode case in Fe@C_{80} due to the changed coupling to the semi-metallic graphene leads. HOMO-related transmission peaks are more distinct for Co@C_{80} and Ni@C_{80}, indicating greater electronic coupling in the filled states. Resonance peaks near the gap edges are more distinct in the graphene-joined junctions, indicating greater energy selectivity in transport. In C_{80} for both electrodes, the HOMO and LUMO remain split with low transmission in the gap, serving as a baseline reference. The metal dopants enhance transmission and close the gap, especially under gold contacts. Ni@C_{80} shows enhanced transmission near the LUMO level in both configurations, which suggests that it can support n-type conduction. The difference in electrode type produces a difference in level alignment, with gold providing broader and smoother transmission profiles, and graphene producing sharper and more localized transmission features[36]. The present NEGF–DFT calculations neglect explicit electron–phonon interactions and focus on coherent elastic charge transport. This approximation is commonly employed for molecular-scale devices under low-bias and near-equilibrium conditions, where transport is primarily governed by the electronic structure and molecule–electrode coupling. For the studied system, vibrational effects are expected to mainly cause quantitative renormalization of conductance rather than qualitative changes in the observed transport behavior. Nevertheless, at higher bias voltages or elevated temperatures, electron–phonon coupling may influence inelastic scattering and energy dissipation. Incorporating these effects using inelastic NEGF formalisms constitutes an important direction for future work.

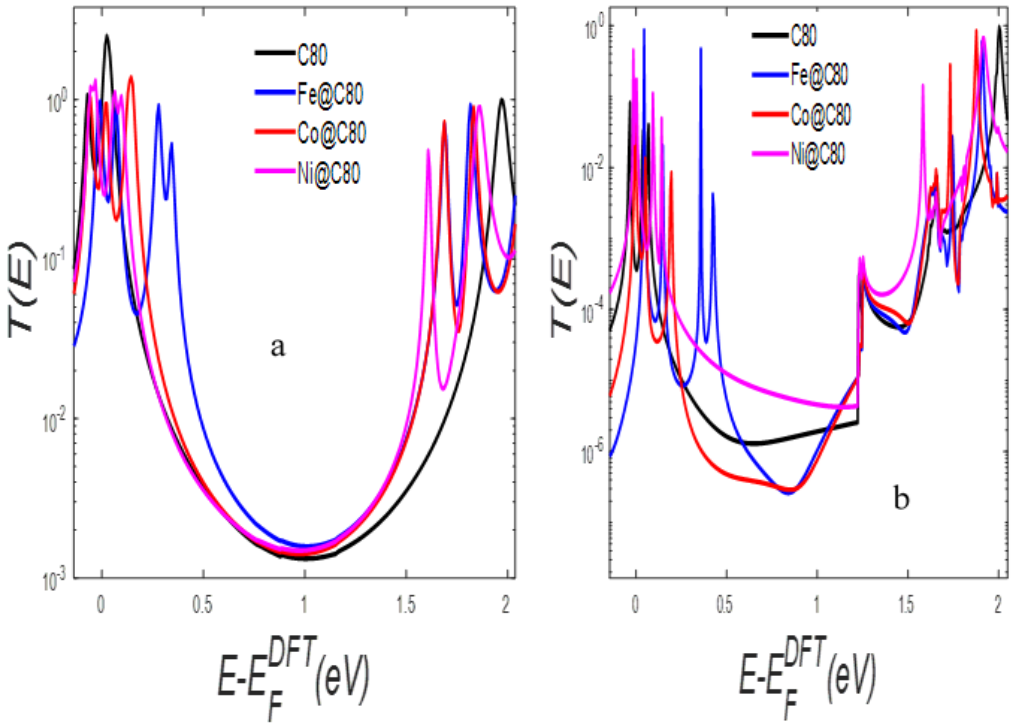

Figure 4: The transmission coefficient T(E) for molecular junction connected to (a) gold and (b) graphene electrodes.

The logarithmic electrical conductance log(G/G0) response of M@C_{80} (M = Fe, Co, Ni) at gold and graphene electrodes is presented in Figure 5(a,b). For figure 5(a), the respective conductance of pure C_{80} drops sharply between 0.5–1.5 eV, corresponding to a low-conductance regime likely owing to the energy gap. When Fe, Co, or Ni atoms are encapsulated in the C_{80} cage, the conductance curves are elevated and shifted, particularly in the energy range of 0.2–0.8 eV. Fe@C_{80} shows a prominent peak at slightly less than 0.2 eV, suggesting that new states by Fe doping at or near the Fermi level enhance electron transmission. Co@C_{80} also shows a more durable, higher conductance than pristine C_{80} in the 0.5–1.5 eV range, suggesting moderate improvement through Co doping. Ni@C_{80} demonstrates the most significant increase in conductance beyond 1.2 eV, with more rounded and broader features, pointing toward improved high-energy transport capability. These results confirm that gold electrodes form effective coupling with the fullerene cage, and the insertion of transition metals introduces states inside the transport gap useful for charge conduction.

As shown in Fig. 5(b), Co@ C_{80} shows the weakest electrical conductivity in the 0.5–1.2 eV energy range, compared to pristine C_{80} and the other endohedral complexes. Fe@C_{80} is significantly improved, especially below 0.5 eV, with a maximum at 0.2 eV, which may be ascribed to Fe-induced states falling on the Dirac point of graphene. Co@C_{80} has a flatter, more subdued conductance that speaks to poor electron transmission and poor orbital overlap. Ni@C_{80} is slightly superior to Co with higher conductance at energies higher than 1 eV and a dramatic jump at around 1.5 eV. Still, none of the doped systems used in graphene electrodes surpass their gold equivalents in conductance levels. These findings show that both electrodes are boosted by doping, but gold has a better ability to sustain strong coupling and orbital hybridization with the molecule. Among the dopants, Fe is always found to have maximum conductance at the Fermi level,

and therefore Fe@C_{80} seems to be the best choice for device applications[37]. Generally, gold electrodes perform better than graphene in attaining maximum conductance in M@C_{80} molecular junctions.

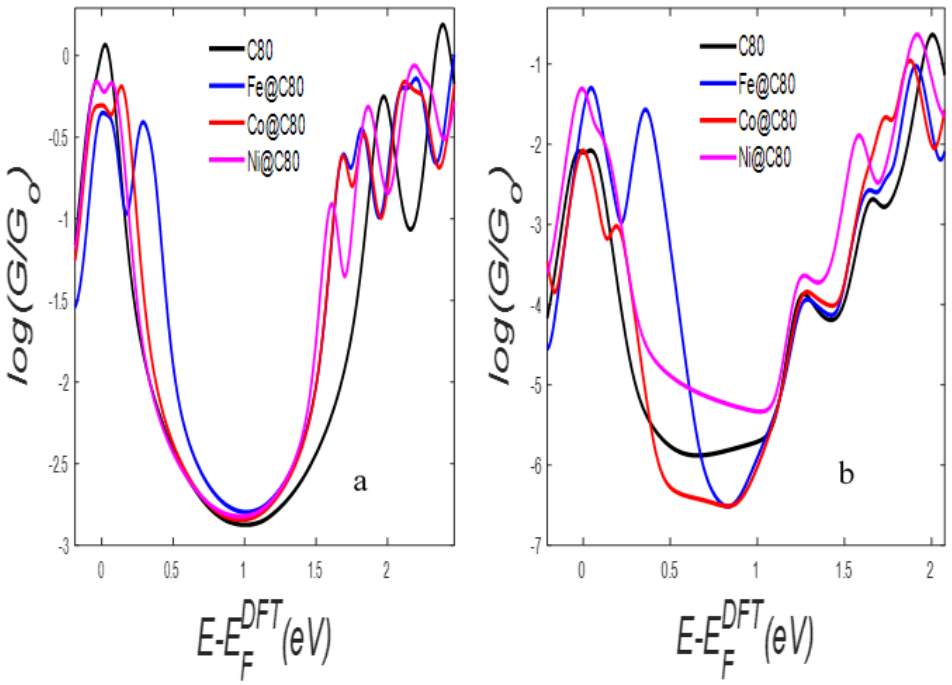

Figure 5: The logarithmic electrical conductance log(G/G_0) behavior of molecular junction with gold and graphene electrodes.

The Seebeck coefficient S(μV/K), as indicated in Figure 6 (a,b) for M@C_{80} (M = Fe, Co, Ni) molecular junctions, is sensitively determined by the encapsulated metal atom and the electrode material. In Figure 6a, for gold electrodes, Seebeck curves for all systems oscillate about zero, and distinct peak and dip structures indicate variations of electronic transmission asymmetry close to the Fermi level. Fe@C_{80} shows sharp oscillations with the highest positive peak at +200 μV/K around 0.5 eV, and an extremely deep negative valley around −0.25 eV, which reflects strong energy-dependent transport characteristics. Co@C_{80} also shows a large thermopower response with less oscillatory and smooth oscillations with a high peak around 0.4 eV. Ni@C_{80} shows more stabilized oscillations with narrower peaks, especially between −0.5 and 0.5 eV, which reflect moderate thermoelectric behavior. Compared to pristine C_{80}, most doped C_{80} systems exhibit enhanced Seebeck coefficients within specific energy regions around the Fermi level, although this enhancement is not universal for all dopants, as evidenced by the Ni@C_{80}[38].

In Figure 6b, for graphene electrodes, Seebeck values are of larger magnitudes by orders of magnitude, with Fe@C_{80} reaching values of up to ±600 μV/K, so that graphene allows more intense sensitivity of thermopower to molecular energy level modulation. The Fe@C_{80} curve possesses a large negative peak around −0.2 eV and a strong positive spike just above 0.5 eV, reflecting an extremely highly asymmetric transmission spectrum optimal for maximum thermoelectric efficiency. Co@C_{80} has smoother but larger oscillations, with positive and negative values over a wider range, while Ni@C_{80} has smaller amplitude oscillations, indicating lower thermopower sensitivity. Notably, graphene-based systems have wider Seebeck features than gold, likely because graphene's weaker but more selective coupling to the molecular orbitals is accountable[39]. This results in greater transmission slope contrasts, elevating the Seebeck coefficient. Although the absolute Seebeck coefficients are greater with graphene, the stability and control

of gold electrodes may be preferable in practical applications. Among all the dopants, Fe consistently demonstrates the largest thermopower response with both electrodes and, therefore, is an extremely promising candidate for thermoelectric applications. Generally, the electrode choice significantly impacts Seebeck behavior: graphene increases the thermoelectric voltage to its maximum because of improved energy filtering. At the same time, gold gives more symmetrical and stable output.

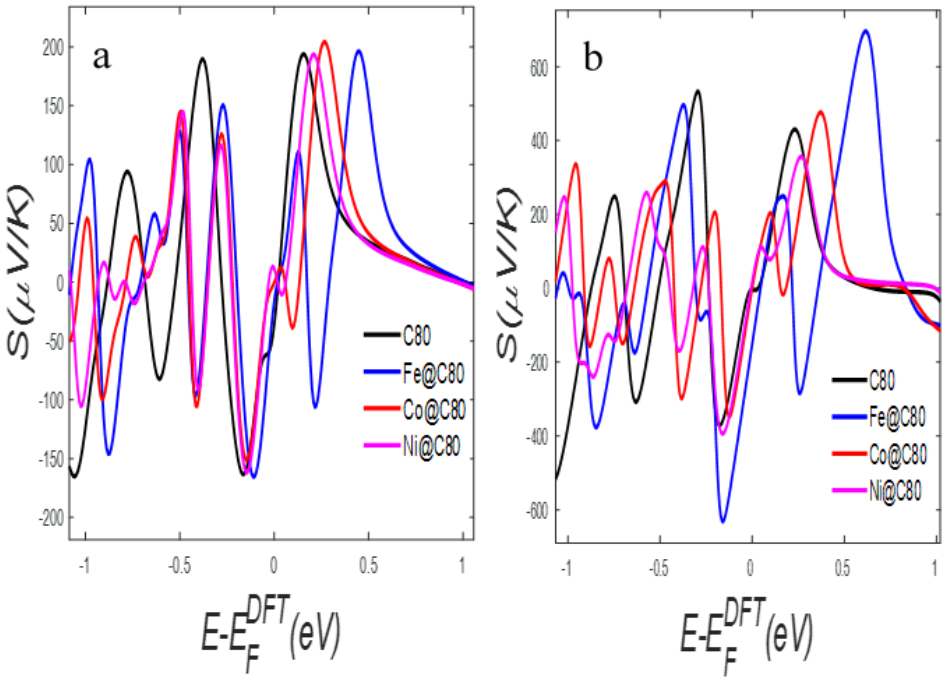

Figure 6: The Seebeck coefficient S(μV/K) for molecular junctions connected to both gold and graphene electrodes.

Fig. 7(a,b) presents the M@C_{80} (M = Fe, Co, Ni) molecular junction thermoelectric figure of merit (ZT) compared to Pristine C_{80}, with (a) gold and (b) graphene electrodes. The figure (7a) ZT values are fairly moderate and display numerous sharp peaks between the energy range of −1 to 1 eV, indicating resonance-like improvements of the thermoelectric characteristics concerning localized states and good transmission characteristics. Pristine C_{80} has a broad and low ZT profile, with metal encapsulation generally adding several new peaks, with Ni@C_{80} reaching values close to 1.5, showing greater thermoelectric efficiency. Co@ C_{80} shows a higher ZT than pristine C_{80} at the Fermi level, reflecting the positive effect of transition-metal doping on thermoelectric efficiency when in contact with gold, while Fe@ C_{80} displays ZT enhancement at energies away from the Fermi level.

Figure (7b) shows larger ZT values more than 1000 near −1 eV with graphene electrodes for Co@C_{80}. When using the NEGF–DFT framework to evaluate the thermoelectric properties of the Co@C_{80} molecular junction coupled to graphene electrodes, the figure of merit ZT should be interpreted within a quantum coherent transport picture rather than in the conventional bulk sense. In this approach, the electrical conductance, Seebeck coefficient, and electronic thermal conductance are all derived from the energy-dependent transmission function T(E) , making ZT highly sensitive to the presence of sharp and asymmetric transmission features near the Fermi level. In Co@C_{80} graphene junctions, localized Co d-states can induce narrow resonances close to E_F, which may strongly enhance the Seebeck coefficient while simultaneously

suppressing the electronic thermal conductance, leading to very large calculated ZT values. Such high ZT values, potentially reaching hundreds or even larger in purely electronic NEGF calculations that reflect an idealized transport regime analogous and do not imply a violation of thermodynamic principles[40]. Even in this limit, the thermoelectric efficiency remains strictly bounded by the Carnot efficiency. Moreover, these large ZT values should be regarded as upper theoretical limits, since phonon thermal conductance, inelastic scattering, and level broadening at the graphene contacts effects often neglected or approximated in coherent NEGF–DFT treatments. Fe@C_{80} displays a notable thermoelectric response with a maximum ZT enhancement close to 600 at around − 0.1 eV. Ni@C_{80} and C_{80} have rather subdued response with ZT being less than 50 throughout the range. Although the Co atom is encapsulated inside the C_{80} cage and does not directly couple with the graphene π-orbitals, it strongly modifies the electronic structure of the fullerene cage, creating sharp localized states near the Fermi level[41]. These states affect the C_{80} molecular orbitals, which interact with the extended π-states of the graphene electrode through π-π coupling. The strong transmission resonance and steep transmission slope near −1 eV caused by this indirect but strong coupling result in a significant increase in the Seebeck coefficient and ZT value. Thus, the Co-induced molecular orbital modifications inside the cage and the π-π interactions between the graphene electrode and the fullerene cage orbitals work in concert to produce the intense resonance.

Fe@C_{80} and Ni@C_{80}, on the other hand, have a number of metal-induced states that are either more distant from the Fermi level or couple with graphene less successfully, which results in wider transmission features and poorer thermoelectric performance. Graphene producing significantly higher ZT values due to its high mobility and superior energy filtering capability. These results show that electrode material selection meaningfully affects thermoelectric performance[42]. The extremely high ZT values reported by graphene electrode promise superior thermoelectric efficiency in nanoscale devices.

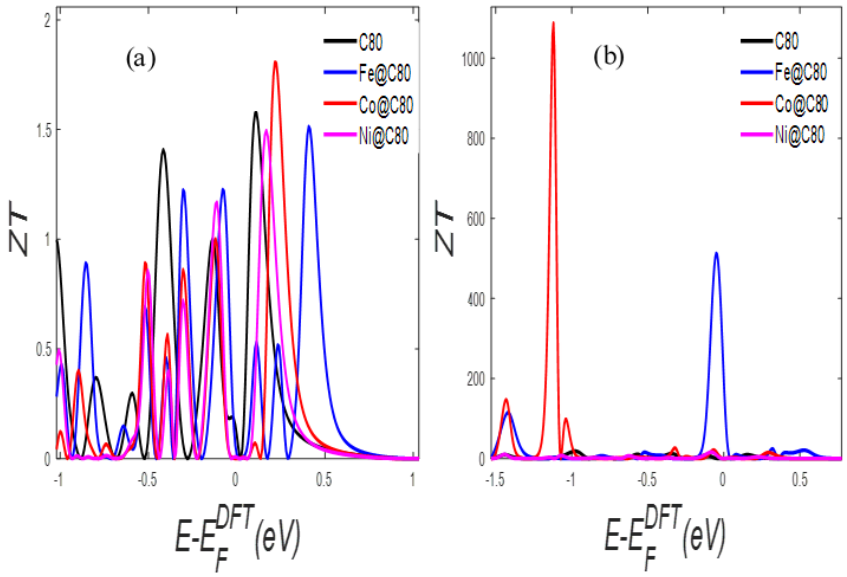

Figure 7: The thermoelectric figure of merit (ZT) of Molecular junctions attached to (a) gold and (b) graphene electrodes.

Figure 8(a,b) indicates power factor (PF) profiles of pristine C_{80} and M@C_{80} (M = Fe, Co, Ni) molecular junctions with gold and graphene electrodes, respectively. Figure 8(a) shows the highest PF peaks, with values above 9.5×10^4 pW/K², especially in the energy around 0.1 eV. The PF is suppressed by the insertion of transition metals, suggesting that changes in the density of states or scattering effects affect charge carrier

transport. Ni@C_{80} and Co@C_{80} display a number of peaks with moderate amplitudes among the doped systems, indicating a compromise between S and σ in specific localized energy intervals. When used with gold contacts, Fe@C_{80} displays comparatively low PF values with fewer high peaks, suggesting limited enhancement.

The PF behavior of the same systems, however, with graphene electrodes is depicted in Figure (b). The tendency here is very different: the highest and most peaked PF is still found in pristine C_{80}, with a peak PF of roughly 8000 pW/K² at −0.5 eV. Ni@C_{80} and Co@C_{80} show improved PF close to the Fermi level, suggesting improved synergy with graphene electrodes by effective energy filtering or electronic coupling. Fe@C_{80} continues to show moderate PF values, showing that it is less sensitive to changes in electrode material. The broader PF peaks in the graphene junctions reveal more delocalized states and smoother transport profiles across energy levels[43,44]. Graphene provides a better platform for thermoelectric enhancement in doped systems, especially where π–π interactions and extended electronic states are implicated than gold[45]. Overall, graphene-based junctions yield a longer and more tunable PF profile, particularly for Ni@C_{80} and Co@C_{80}, and are thus more likely to be utilized in thermoelectric devices at the nanoscale.

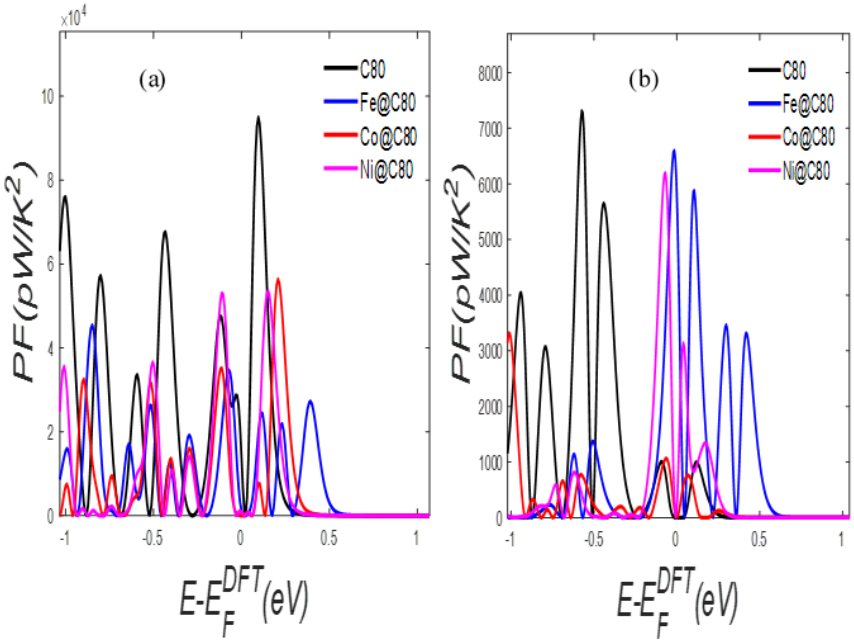

Figure 8: The power factor (PF) profiles of molecular junctions connected to gold and graphene electrodes.

Figures 9(a,b) present the temperature-dependent thermal conductivity (κ) of M@C_{80} (M = Fe, Co, Ni) molecular junctions concerning pristine C_{80}, in gold and (b) graphene electrodes contact. In Figure 9(a), for gold electrodes, thermal conductivity with temperature increases first, reaches a peak, then decreases gradually. Among the compounds, Ni@C_{80} displays the highest κ, up to 3.7×10^{-10} W/m·K at around 300 K, which indicates enhanced phonon or electron conducting paths through the Ni dopant. Co@C_{80} and C_{80} have high κ, with Co@C_{80} up to 3.3×10^{-10} W/m·K. The lowest thermal conductivity for the gold-electrode system is for Fe@C_{80}, suggesting more phonon scattering or limited thermal transport channels[46]. The relative decrease after the maximum is typical and can be attributed to greater phonon–phonon scattering at higher temperatures.

Figure 9(b) shows that the thermal transport in graphene electrode is far lower than gold. Ni@C_{80} has the highest thermal conductivity among graphene-type junctions. It shows a very sharp peak around 8×10^{-12} W/m·K at the temperatures close to 100K followed by a generally steady trend with slight oscillations. Fe@C_{80} and Co@C_{80} maintain low values at all temperatures. C_{80} has significant κ peaking at 3.5×10^{-12} W/m·K. Saturation of κ indicates either stronger energy filtering effects or weaker electron–phonon coupling, which may facilitate charge transfer and delay heat transport[47]. The decreased thermal conductivity of graphene can help minimize heat dissipation in thermoelectric devices. Therefore, while gold provides increased thermal conductivity and better heat spreading, graphene offers a better platform for thermoelectric applications where low κ is required.

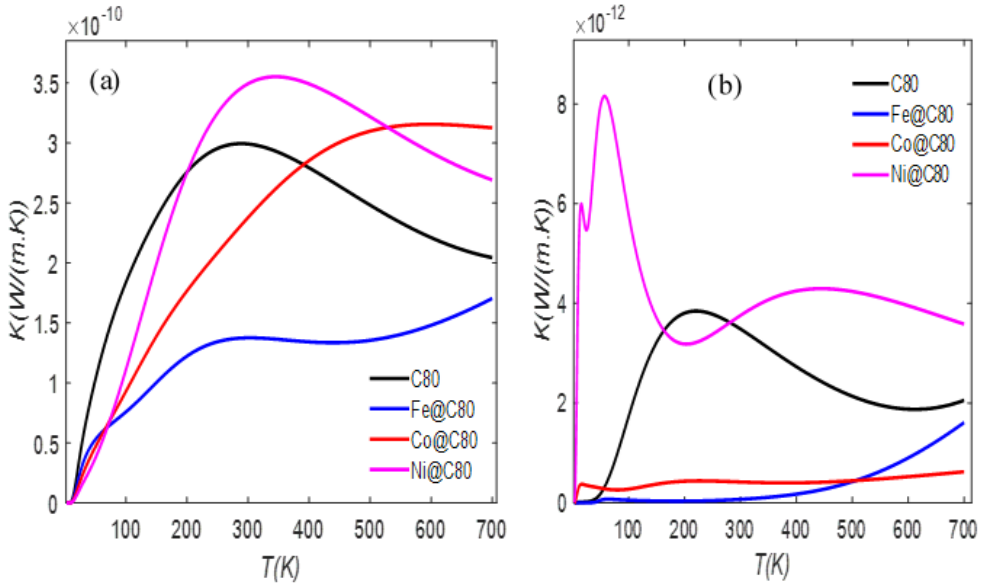

Figure 9: The thermal conductivity (κ) of molecular junctions with (a) gold and (b) graphene electrodes.

Figure 10(a-c) Show the energy dependence of spin-polarized transmission in endohedral fullerenes with a gold electrode. In (Fig.9a) Fe@C_{80} the spin-up (black line) shows a number of sharp peaks near the Fermi level corresponding to several states contributing a remarkable amount to the electron transport channels whereas the spin-down channel displays low transmission intensities throughout the most part of the energy range, showing strong spin polarization in Fe@C_{80}. This spin asymmetry indicates that the doped Fe enhances magnetic exchange interactions within the fullerene cage, thereby favoring spin-selective transport[48]. In (Fig.9b), for Co@C_{80}, the spin-up and spin-down channels both possess more balanced transmission profiles with a number of overlapping peaks; however the spin-up component still displays higher intensity near −0.2 eV. The transmission (green line) of Co@C_{80} is comparatively smoother compared to that of Fe@C_{80}, reflecting a reduction in the spin splitting upon encapsulation of Co. The presence of distinct peaks for both spins in Co@C_{80} reflects moderate spin filtering ability but lower dominance compared to Fe@C_{80}. In (Fig.9c), very similar transmission profiles for spin-up and spin-down states in Ni@C_{80} reflect no appreciable spin polarization effects. The maximum overlap of Ni@C_{80} shows that the magnetic moment of Ni is greatly quenched due to interaction with the carbon cage and gold electrode. In each of the three systems, the sharp transmission peaks correspond to molecular orbitals close to the Fermi energy, enabling resonant tunneling. Fe@C_{80} shows the strongest contrast between spin-up and spin-down channels, and thus the strongest candidate for application to spintronics among the three[49]. The transmission magnitude for Fe@C_{80} approaches unity at particular energies, indicating strong coupling of the molecule to the gold electrode[50]. Co@C_{80} displays intermediate character, with moderate spin-

dependent characteristics but lower contrast to that of Fe@C_{80}. Ni@C_{80}, with nearly symmetric spin transport, is nearly a non-magnetic molecule in these conditions. This observation adequately suggests how the choice of encapsulated metal affects the spin polarization and transport properties of the fullerene system. Additionally, peak broadening in Co@C_{80} and Ni@C_{80} compared to Fe@C_{80} reveals differences in hybridization strength and electron scattering at the molecule–electrode interface. The graph also shows that for all the systems, the most significant transport channels are within ±0.5 eV of the Fermi level, i.e., the energy range of interest relevant to low-bias device operation. Fe@C_{80} has the highest possibility for spin-selective current, moderate spin sensitivity arises from Co@C_{80}, and Ni@C_{80} is close to spin-degenerate transport behavior.

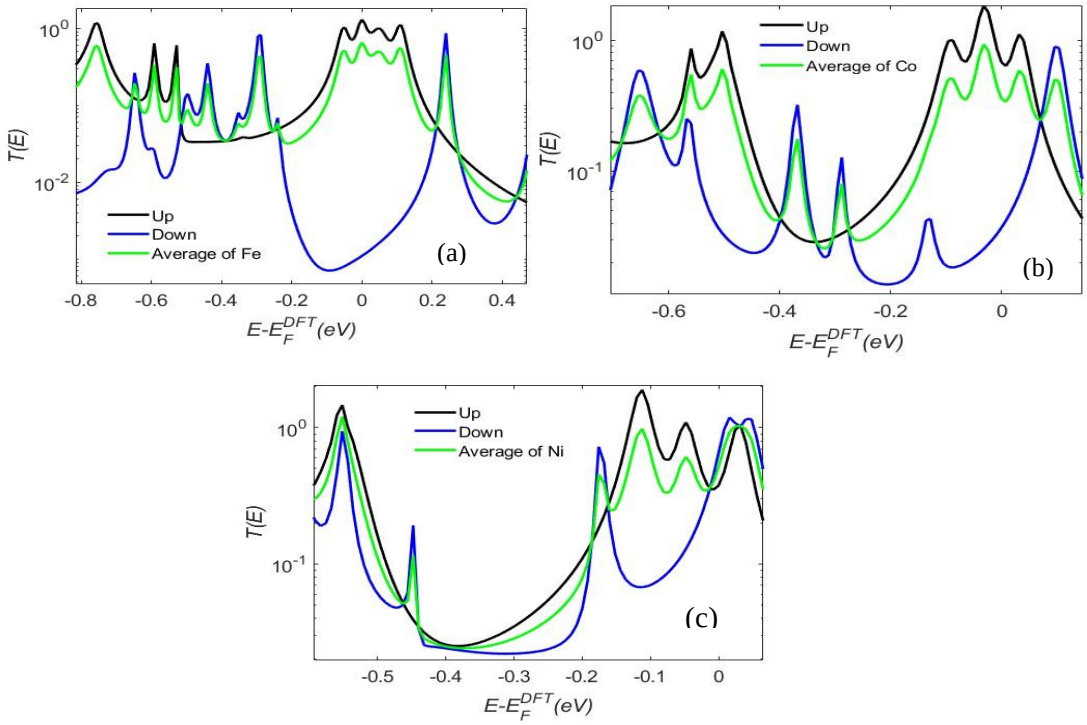

Figure 10: The spin-dependent transmission spectra as a function of energy for endohedral fullerenes connected to a gold electrode.

Conclusion:

Designing molecular junctions that offer adjustable spin- and thermoelectric response is critical in nanoscale device applications. We examine M@C_{80} (M = Fe, Co, Ni) connected to gold and graphene electrodes using density functional theory (DFT) and non-equilibrium Green's function methods. The ability of transition metals encapsulated in fullerene cages to induce charge transfer, spin splitting, and orbital hybridization creates favorable transport conditions. For example, Au–Fe@C_{80}–Au junctions show incredibly strong spin polarization and near unity transmission at the Fermi level, which is ideal for spintronic applications. Alternatively, Gr–Co@C_{80}–Gr presents a remarkable thermoelectric figure of merit (ZT > 1000) as a result of sharp transmission resonances combined with effective π–π interaction with the graphene electrode. These values represent upper theoretical limits within a coherent electronic transport regime and do not imply a violation of thermodynamic constraints, as the thermoelectric efficiency remains bounded by the Carnot limit. Remarkably, gold electrodes produce strong coupling with higher conductance, while graphene electrodes show better energy filtering along with improved thermopower. In

conclusion, M@C_{80} molecular junction structures can be developed for high-performance spintronic and thermoelectric devices.

Statements and Declarations

Author Contributions: Alaa A. Al-Jobory and Sameer Nawaf wrote the main manuscript text. Anhar Ouda made the computational part, Ali Ismael reviewed the final drafts. All authors contributed to the manuscript and agreed to publish it.

Data Availability: The data supporting this study's results are available from the corresponding author upon reasonable request.

Competing Interest: The authors declare no competing interests.

Funding: The authors declare that no funds were received during the preparation of this manuscript.

Acknowledgement: The authors would like to express their truthful appreciation to the staff of the Theoretical Physics Laboratory at the Department of Physics, College of Science, University of Anbar. There useful discussions contributed to the successful completion of this research.

References:

[1] Syduzzaman M, Hassan A, Anik H R, Akter M and Islam M R 2023 Nanotechnology for high-performance textiles: a promising frontier for innovation *ChemNanoMat* **9** e202300205

[2] Parker M C and Jeynes C 2020 Fullerene stability by geometrical thermodynamics *ChemistrySelect* **5** 5–14

[3] Oda A A, Al-jobory A A, Nawaf S, Lattoofi N F and Motlak M 2025 Electrode variability and its impact on the characteristics of M @ C 80 molecular junctions (M = P , S , As , Se) *Mater. Sci. Semicond. Process.* **199** 109822

[4] Acquah S F A, Penkova A V., Markelov D A, Semisalova A S, Leonhardt B E and Magi J M 2017 Review—The Beautiful Molecule: 30 Years of C 60 and Its Derivatives *ECS J. Solid State Sci. Technol.* **6** M3155–62

[5] Oda A A and Al-Jobory A A 2025 Effect of electrode type on electric and thermoelectric properties of M@ C60: M= P, As, and Se *Int. J. Mod. Phys. B* 2550140

[6] Motlak M, Al-Jobory A A, Hamza A and Nawaf S 2025 Production of Se-nanorods-rGO nanocomposite for use as a counter electrode in dye-sensitized solar cells *J. Sol-Gel Sci. Technol.* **115** 162–70

[7] Mohammad A-T, Mahdi H A, Mahdi M A and Ameen W A 2025 Novel liquid crystal star-shaped based coumarin: Synthesis, characterization, phase behaviors and photoluminescence studies with DFT analysis *J. Mol. Liq.* **426** 127371

[8] Khalaf A M, Motlak M, Humadi M A, Rzaij J M, Nawaf S and Their O M 2025 First-principles analysis on the electronic structure, magnetic and optical properties of Fe-incorporated boron nitride zigzag nanotubes *Int. J. Mod. Phys. B* **39** 1–12

[9] Nawaf S, Ibrahim A K and Al-Jobory A A 2023 Electronic structure and optical properties of Fe-doped TiO2 by ab initio calculations *Int. J. Mod. Phys. C* **34** 2350016

[10] Nawaf S, Rzaij J M, Al-Jobory A A and Motlak M 2024 Investigating the optical properties and electronic structure of gallium phosphide nanotubes doped with arsenic via implementing first-principles calculations *J. Mol. Model.* **30** 243

[11] Motlak M, Hamza A and Nawaf S 2019 Synthesis and application of Co/TiO2 nanoparticles incorporated carbon nanofibers for direct fuel cell *J. Phys. Conf. Ser.* **1178**

[12] Motlak M, Nawaf S and Al-Jobory A A 2025 Investigation impact of (Ni, Cu) co-doping on the electronic, optical, magnetic, and I-V characteristics of GaP nanosheets *J. Mol. Model.* **31** 139

[13] Oda A and Al-Jobory A 2024 Investigate the electrical and thermoelectric properties of M@C60 where (M=Co, Ni): A DFT study *J. Univ. Anbar Pure Sci.* **18** 219–22

[14] Sarfaraz S, Yar M and Ayub K 2024 The electronic properties, stability and catalytic activity of metallofullerene (M@ C60) for robust hydrogen evolution reaction: DFT insights *Int. J. Hydrogen Energy* **51** 206–21

[15] Caliskan S 2019 A first principles study on spin resolved electronic properties of X@ C70 (X= N, B) endohedral fullerene based molecular devices *Phys. E Low-dimensional Syst. Nanostructures* **108** 83–9

[16] He T, Gao G, Kou L, Will G and Du A 2017 Endohedral metallofullerenes (M@C60) as efficient catalysts for highly active hydrogen evolution reaction *J. Catal.* **354** 231–5

[17] Tawfik S A, Cui X Y, Ringer S P and Stampfl C 2016 Endohedral metallofullerenes, M@C60 (M = Ca, Na, Sr): selective adsorption and sensing of open-shell NOx gases *Phys. Chem. Chem. Phys.* **18** 1–8

[18] Masaki Takata, Buntaro Umeda, Eiji Nishibori, Makoto Sakata, Yahachi Saitot M O & H S 1995 Confirmation by X-ray diffraction of the endohedral nature of the metallofullerene Y@C82 *Nature* **377** 46–49

[19] Nakagawa A, Nishino M, Niwa H, Ishino K, Wang Z, Omachi H, Furukawa K, Yamaguchi T, Kato T, Bandow S, Rio J, Ewels C, Aoyagi S and Shinohara H 2018 Crystalline functionalized endohedral C60 metallofullerides *Nat. Commun.* **9**

[20] Khudhair A A, Mazhir S N and Hammed M G 2024 Optical and structural characterization of Au@ ZnO core–shell nanoparticles prepared by pulsed laser ablation as anticancer agents for skin cancer *J. Opt.* 1–10

[21] Nawaf S, Al-Jobory A A, Rzaij J M and Ibrahim A K 2024 First Principal Calculations on the Electronic Structure and the Optical Properties of Al-doped Zigzag GaN Nanotube *Plasmonics* **19** 3035–3042

[22] Al-Jobory A A, Nawaf S and Motlak M 2025 Investigation of the optical and electrical structure of Al1-xInxN alloys: A DFT study *Electron. Struct.* **7** 015002

[23] Soler J M, Artacho E, Gale J D, García A, Junquera J, Ordejón P and Sánchez-Portal D 2002 The SIESTA method for ab initio order-Nmaterials simulation *J. Phys. Condens. Matter* **14** 2745

[24] Ferrer J, Lambert C J, García-Suárez V M, Manrique D Z, Visontai D, Oroszlány L, Rodríguez-Ferradás R, Grace I, Bailey S W D and Gillemot K 2014 GOLLUM: a next-generation simulation tool for electron, thermal and spin transport *New J. Phys.* **16** 93029

[25] Alshammari M, Al-Jobory A A, Alotaibi T, Lambert C J and Ismael A 2022 Orientational control of molecular scale thermoelectricity *Nanoscale Adv.* **4** 4635–8

[26] Nawaf S, Al-Jobory A A, Ouda A A and Najm R A 2025 Thermoelectric performance enhancement in cadmium-combined GaN nanosheets *Dalt. Trans.* **54**

[27] Mollaamin F and Monajjemi M 2025 Application of nanoscale boron nitride for encapsulation of noxious transition metals (Cr, Mn, Fe, Zn, W, Cd) in soil: Physico-chemical characterization using DFT modeling *Adv Phys Res* **7** 5–28

[28] Yamada M, Akasaka T and Nagase S 2010 Endohedral metal atoms in pristine and functionalized fullerene cages *Acc. Chem. Res.* **43** 92–102

[29] Motlak M, Nawaf S and Al-Jobory A A 2025 Dual-Doping Effects of (Cu, Co) on the Optoelectronic Properties of Rutile TiO2 Nanomaterials *ChemistrySelect* **10** e04996

[30] Al-Jobory A A and Ismael A K 2023 Controlling quantum interference in tetraphenyl-aza-BODIPYs *Curr. Appl. Phys.* **54** 1–4

[31] Lu T and Chen F 2012 Multiwfn: A multifunctional wavefunction analyzer *J. Comput. Chem.* **33** 580–92

[32] Lu T 2024 A comprehensive electron wavefunction analysis toolbox for chemists, Multiwfn *J. Chem. Phys.* **161**

[33] Lambert C J 2015 Basic concepts of quantum interference and electron transport in single-molecule electronics *Chem. Soc. Rev.* **44** 875–88

[34] Ameen W A, Walet N R and Xian Y 2017 Electronic correlations in the Hubbard model on a bi-partite lattice *Ann. Phys. (N. Y).* **378** 280–302

[35] Sreeprasad T S and Berry V 2013 How do the electrical properties of graphene change with its functionalization? *small* **9** 341–50

[36] Xu Y and Liu J 2016 Graphene as transparent electrodes: fabrication and new emerging applications *Small* **12** 1400–19

[37] Feng S, Lin Z, Gan X, Lv R and Terrones M 2017 Doping two-dimensional materials: ultra-sensitive sensors, band gap tuning and ferromagnetic monolayers *Nanoscale Horizons* **2** 72–80

[38] Wang X, Ismael A, Alanazi B, Al-Jobory A, Wang J and Lambert C J 2023 High Seebeck coefficient from isolated oligo-phenyl arrays on single layered graphene via stepwise assembly *J. Mater. Chem. C* **11** 14652–60

[39] Sang M, Shin J, Kim K and Yu K J 2019 Electronic and thermal properties of graphene and recent advances in graphene based electronics applications *Nanomaterials* **9** 374

[40] Martinez A and Barker J R 2020 Quantum transport in a silicon nanowire FET transistor: hot electrons and local power dissipation *Materials (Basel).* **13** 3326

[41] Karle N N 2017 *DFT Study of Adsorption of Trimetallic Endohedral Fullerenes on Graphene* (The University of Texas at El Paso)

[42] Yang L, Chen Z, Dargusch M S and Zou J 2018 High performance thermoelectric materials: progress and their applications *Adv. Energy Mater.* **8** 1701797

[43] Yu H, Kutana A and Yakobson B I 2016 Carrier delocalization in two-dimensional coplanar p–n

junctions of graphene and metal dichalcogenides *Nano Lett.* **16** 5032–6

[44] Dollfus P, Nguyen V H and Saint-Martin J 2015 Thermoelectric effects in graphene nanostructures *J. Phys. Condens. Matter* **27** 133204

[45] Amollo T A, Mola G T, Kirui M S K and Nyamori V O 2018 Graphene for thermoelectric applications: prospects and challenges *Crit. Rev. Solid State Mater. Sci.* **43** 133–57

[46] Park S, Jang J, Kim H, Park D Il, Kim K and Yoon H J 2020 Thermal conductance in single molecules and self-assembled monolayers: Physicochemical insights, progress, and challenges *J. Mater. Chem. A* **8** 19746–67

[47] Zeng Y, Wu D, Cao X, Zhou W, Tang L and Chen K 2020 Nanoscale organic thermoelectric materials: measurement, theoretical models, and optimization strategies *Adv. Funct. Mater.* **30** 1903873

[48] Sun S, Zhang Y, Shi X, Sun W, Felser C, Li W and Li G 2024 From charge to spin: an in-depth exploration of electron transfer in energy electrocatalysis *Adv. Mater.* **36** 2312524

[49] Inomata K, Ikeda N, Tezuka N, Goto R, Sugimoto S, Wojcik M and Jedryka E 2008 Highly spin-polarized materials and devices for spintronics *Sci. Technol. Adv. Mater.* **9** 14101

[50] Weber K, Hockett L and Creager S 1997 Long-range electronic coupling between ferrocene and gold in alkanethiolate-based monolayers on electrodes *J. Phys. Chem. B* **101** 8286–91